SSRG International Journal of Electrical and Electronics Engineering
ISSN: 2348-8379 / https://doi.org/10.14445/23488379/IJEEE-V10I2P103

Volume 10 Issue 2, 19-34, February 2023

Original Article

Optimized FOPID Controller for Transient Stability Improvement in a Microgrid with Energy Storage

C. Srisailam[1], M. Manjula[2]

[1, 2]*Department of Electrical and Electronics Engineering, University College of Engineering, Osmania University, Telangana, India*

[1]*Corresponding Author: srisailam.be@gmail.com*

Received: 28 December 2022 Revised: 04 February 2023 Accepted: 13 February 2023 Published: 28 February 2023

Abstract *- Recently, Direct current (DC) microgrids have gained immense popularity due to their dependable and efficient framework, as well as their high transmission efficiency and low electric power conversion. However, the non-linear nature of Renewable Energy Sources (RESs), the increased presence of power electronic devices and sudden load changes leads to the onset of stability issues in the DC microgrid. Thereby, a DC microgrid structure including Photovoltaics (PV) system, Doubly Fed Induction Generator (DFIG) based Wind Energy Conversion System (WECS) and Energy Storage System (ESS) with suitable control approaches is proposed with the aim of enhancing the voltage stability. Here, a higher order Boost converter is employed with Grey Wolf Optimization (GWO) assisted Fractional Order Proportional Integral Derivative (FOPID) controller for enhancing and stabilizing the PV output. The DFIG-based WECS is interfaced to the DC bus using a Pulse Width Modulation (PWM) Rectifier, which in turn is controlled using a Proportional Integral (PI) Controller. The ESS, which optimizes the power flow in the microgrid, comprises of battery and an Isolated Bidirectional Converter (BDC). The generated power from both WECS and PV is supplied to a utility grid via a three-phase Voltage Source Inverter (3φ VSI), while the grid voltage synchronization is achieved using a PI controller. The proposed microgrid structure is simulated in MATLAB to ascertain its performance, and an excellent efficiency of 98.4% is observed.*

Keywords *- PV system, DFIG based WECS, Higher order boost converter, GWO-assisted FOPID controller, ESS, Isolated BDC, PI controller.*

1. Introduction

Electrical energy is regarded as the backbone that facilitates and supports the functioning of the modern world. As a matter of fact, its ample availability is crucial for the growth and development of the entire human society. The primary sources of electrical energy, which are the conventional energy sources, have been declining globally at an alarming rate, prompting nations to make crucial environmental and economic decisions towards developing Renewable Energy Sources. Moreover, the threat of global warming has also triggered the extensive installation of RESs, since it reduces the use of conventional energy sources that emit harmful greenhouse gases [1-3]. Thus, the drastic shift seen in the global power market has contributed to the decentralization of the power sector through increased penetration of RESs at the distribution level, thereby stimulating the expansion of microgrids. The microgrid, which is designed primarily for supplying power to regions dissociated from the central electric system, combines several Energy Storage Systems (ESSs), Distributed Energy Resources (DERs) and loads in its topology [4, 5]. The DC microgrid is the most promising choice among the different microgrid types (DC, AC and Hybrid) owing to the DC output characteristic of both RES and ESS. Moreover, the DC-DC interfaces have higher efficiency as well as better electronic load compliance and problems related to reactive power control and frequency regulation are also evaded [6].

The ESS and RES require the assistance of Power Electronic Converters (PEC) for the purpose of being interfaced with the DC bus of the DC microgrid. Among the various available types of power electronic converters, the DC-DC converters [26, 27] are the most preferred choice in view of their wide availability, better voltage regulation capability, cost-effectiveness and higher efficiency [8], [32]. The DC-DC converters are categorized mainly as isolated and non-Isolated converter configurations. The Boost converter [9], [28], belonging to non-isolated converter topology, is the frequently used converter in PV applications to enhance its output voltage. But this simple converter faces the drawback of lower voltage gain. Hence it is proposed to use a higher-order boost converter with high voltage gain. It aims to improve the PV output voltage applied in this work. Implementing a suitable controller ensures that the output

voltage of the DC-DC converter always remains stable. The conventional PI controller has wide applicability and a simple design, but it is inept at handling disruptions.

Additionally, it also encounters problems such as delayed dynamic response, overshoot and oscillations due to its constant gain values [10]. The PID controller [11, 12] is another commonly used controller in various applications, including instrumentation, flight control, automotive control, motor drive, process control and RES applications. In spite of the advances seen in the field of control theory, almost ninety percent of control loops used in many industrial applications are still PID types [31]. Rather than requiring internal state measurements, these controllers operate on the difference between a controlled parameter and a set reference point, resulting in reduced sensor requirement. However, the PID controller faces certain limitations in handling non-linearities, load and parametric variations. The sliding mode controllers are comparatively better at handling non-linearities, but their liability to chattering phenomena is considered a drawback. The FOPID controller [14-18] [29] is a PID controller extension, and it is based on Fractional calculus. Its distinctive feature lies in its robustness against load variations and non-linearities.

Moreover, it has five tuning parameters, resulting in better control and flexibility while handling distinct design objectives like overshoot, settling time, gain, phase margin and robustness to load variations [34]. The problem of parameter tuning in the FOPID controller is handled using numerical methods, which employ metaheuristic algorithms to optimize cost functions. The Genetic Algorithm (GA) [20], Particle Swarm Optimization (PSO) [21] and Artificial Bee Colony (ABC) [22] are commonly employed for tuning FOPID controllers applied to ensure power electronic converter control. In this work, the GWO algorithm is selected with the intention of adjusting FOPID controller parameters.

The wind energy sector has advanced significantly over the past decade regarding mechanical systems aerodynamic design, PEC, integration with power systems, electric generators and control theory [23]. Among different types of WECS technology, the Wind Turbine (WT) connected to DFIG is prominently used on account of its lower converter ratings with effective power capture owing to variable speed operation [35]. The integration of RESs into the microgrid is facilitated with the application of ESS since it optimises power flow, provides power balance during power shortages and improves grid reliability [25]. This study employs a non-isolated BDC with high power density, symmetrical structure, and soft-switching capability for integrating the ESS into the microgrid.

The superfluous carbon emissions from fossil fuel-powered power plants are the primary causes of global warming and air pollution, which are currently considered the greatest threats our planet faces. In order to keep the earth from becoming totally unfit for human life, a RESs-based microgrid structure encompassing PV-WECS-ESS with suitable control approaches is proposed. Thereby, this work focuses on,

- Developing efficient RESs based microgrid, which aims at minimizing the overdependence on fossil fuels along with reducing the carbon footprint and ultimately reversing the issue of global warming.
- The proposed microgrid includes PV and WECS as the primary power sources since they are sustainable, pollution free and widely available.
- A higher-order Boost converter is employed with GWO assisted FOPID controller in maintaining a constant supply from the PV system.
- The output from the DFIG based WECS is stabilized with the aid of a PI controller.
- The battery is integrated into the DC bus using an Isolated BDC, and the grid voltage synchronization is achieved with the assistance of a PI controller.

The proposed work is verified practically for its effectiveness in maintaining voltage stability using MATLAB software.

2. Proposed System Description

A microgrid structure including PV-WECS-ESS is proposed with novel control approaches in this work, as illustrated in Figure 1. Both PV and WECS are variable power sources that require the implementation of appropriate energy management techniques to ensure reliability and stability when interfaced with the microgrid. The PV system is a low-voltage and intermittent power source that requires a DC-DC converter and controller to enhance its output. Thereby, a higher-order Boost converter of high voltage gain is used to improve its voltage, while a GWO-assisted FOPID controller stabilizes its output voltage. The AC output voltage from DFIG based WECS is converted to DC using a PWM rectifier, whose switching functions are, in turn, controlled using a PI controller.

Since both PV and WECS are intermittent variable sources, an ESS is also included in the proposed work for optimizing the power flow. The ESS also balances the power flow in the microgrid in case of power shortages. An isolated BDC is employed to integrate the battery into the microgrid and allow the bidirectional power flow. The Wind and PV-generated power are fed to the 3φ VSI, through which it is ultimately supplied to the utility grid. The grid voltage synchronization is accomplished by employing a PI controller-based synchronous current controller. MATLAB software is utilized for ascertaining the proposed approach performance.

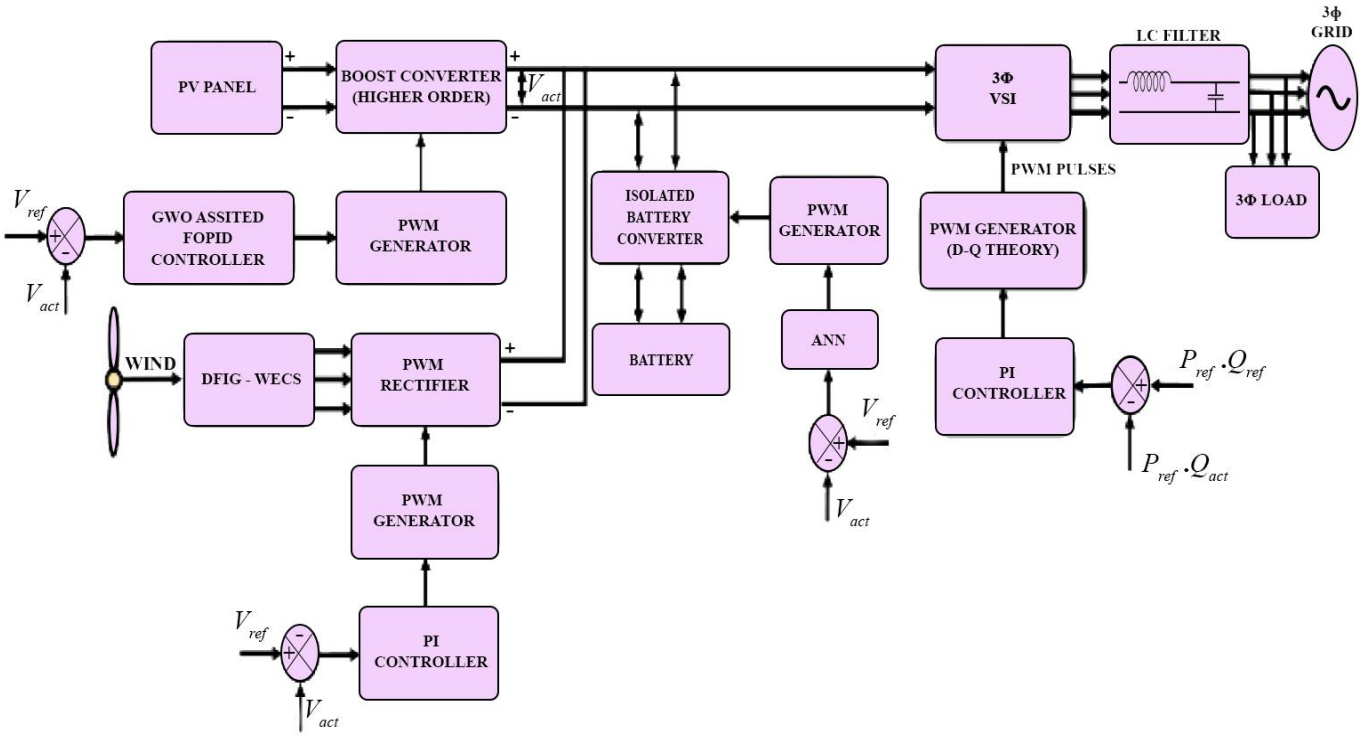

Fig. 1 Proposed DC microgrid structure

3. Proposed System Modelling

3.1. Solar PV Module

PV system output power is determined by the solar intensity that strikes the photovoltaic panels and the crucial criteria supplied by the fabricators. The output power is determined from equation (1) as follows:

$$P_{PV}(t,\beta) = N_S.N_P.V_{OC}(t,\beta).FF(t) \quad (1)$$

$$V_{OC}(t,\beta) = \{V_{OC-STC} - K_V T_C(t)\} \quad (2)$$

In equation (2), V_{OC}=V_{OC-STC}, for ambient temperature conditions, but for different temperatures, V_{OC}will be different for the modules due to$K$.

$$I_{SC}(t,\beta) = \{I_{SC-STC} + K_I[T_C(t) - 25℃]\}\frac{G(t,\beta)}{1000} \quad (3)$$

$$T_c(t) = T_A + (NCOT - 20℃)\frac{G(t,\beta)}{800} \quad (4)$$

Where P_{PV} is the PV module power, t is the time, V_{OC} is the open circuit voltage, V_{OC-STC}, is the standard test condition open circuit voltage, β is the PV module tilt angle, K_V and K_I are the temperature coefficients of short circuit current and open circuit voltage, respectively and N_S and N_P are the total number of PV modules in an array connected in parallel and series and I_{SC} is the short circuit current. FF is the fill factor, where $FF = \frac{V_{max}.\ I_{max}}{V_{OC}.I_S}$. Moreover, I_{Sc} is determined from equation (3) which depends on$K$, and$G$, and G is the global PV module solar irradiance, which depends on daytime and the tilt angle of the solar cell. A PV array total output power consisting of N_S and N_P modules by incorporating efficiency are written as

$$P_{amray}(t,\beta) = \eta_{PV} N_S N_P P_{PV}(t,\beta) \quad (5)$$

Where η_{PV} is the related converter's efficiency of the PV–module. The optimisation technique defines the number of PV modules in parallel, while the DC bus voltage size defines the number of series modules.

3.2. Modelling and Operation of the Proposed Converter

The basic configuration of an active network has a capacitor (C_A) connected to an inductor (L_1) and is powered by an auxiliary switch. When the switch (S_1) is ON, the source charges the inductor, and when S_1 is OFF, the input voltage is twice the voltage across the switchV_{SW}. The input source's voltage is shared equally by C_A andL_1. Several capacitors create the three-stage switched capacitor boost converter C_1, C_2, C_3, C_4, C_5, and C_6 and diodes D_1, D_2, D_3, D_4, and D_5connected in series or parallel at the output of the auxiliary switch, as depicted in Figure 2.

3.2.1. CCM Operation

Only two additional functioning modes are available under the CCM situation. These are modes 1 and 2, respectively, when the auxiliary switch s1 is turned on and

off. Figure 3 depicts the proposed converter's timing diagram, which breaks down the converter circuit's operation into discrete time intervals.

Mode 1(t_0, t_1):

A positive signal is fed to the gate of S_1 during this period, turn the converter ON. The energy begins to be stored by the capacitor and inductor. Figure 4a displays the equivalent circuit. As the proposed converter is regarded to be 0working in ideal mode, the components' internal parasitic resistances are consequently disregarded. During the time interval (t_0, t_1) the circuit parameters are set to zero. Equation (6) gives the voltage caused by the voltage and the inductor stored by the capacitor. The parallel relationship between the DC source,C_A and L_1 can be noticed. In this mode, the inductor current is given by Equation (7).

$$V_{in} = V_{C_A} = V_{L_1} \tag{6}$$

$$I_{L_1} = I_{in} - I_{C_A} \tag{7}$$

Mode 2 (t_1, t_2):

The switch goes off during this time period (t_1, t_2) as depicted in Figure 4b. The inductor dissipates energy while the capacitor (CA) retains the voltage constant. Equation (8) represents the voltage across the switch V_{SW} formulated by applying KVL to the loop. Considering the initial condition from equation (6), the voltage across V_{SW} is given by

$$V_{C_A} + V_{L_1} = V_{SW} \tag{8}$$

$$V_{SW} = 2V_{in} \tag{9}$$

During this interval $D_1$is forward-biased and D_2 is reverse-biased when the inductor is in discharging mode. The capacitor (C_2) is aligned parallel with the switch to produce the appropriate voltage level, as shown in equation (10). Figure 4c represents the equivalent circuit, and the current obtained in this mode is given by equation (11)

$$V_{C_2} = V_{SW} = 2V_{in} = V_{L_1} + V_{C_A} \tag{10}$$

$$i_{C_2} = C_2 \frac{dV_{C_2}}{dt} = i_{L_1} \tag{11}$$

Mode 1 (t_2, t_3):

As S_1 turns on, the converter switches back to mode 1, where the inductors and capacitors continue to operate in their current states while charging, and C_2 continues to hold its charge. During this interval, the voltage across the switch is set to zero as the diode D_1 is reverse biased. The diode D_2 starts to dischargeC_2, which had been charged to the switch voltage level, recharging the capacitor C_1 to the equivalent voltage level. Applying KVL to the equivalent circuit in Figure 4d, the constant output voltage across C1 is obtained.

$$V_{C_2} = V_{C_1} = 2V_{in} \tag{12}$$

The capacitors in the proposed converter pursue the same charging operation and share similar switch voltage. In any particular working mode, if $C_2, C_4, C_6, ,,$ are charging, then $C_1, C_3, C_5, ,,$ be discharging to charge the other side and vice versa.

3.2.2. Converter Gain

It is considered that the output load is coupled acrossC_2. In CCM, the inductor current is assessed by factoring two modes or one whole cycle, and the voltage across the inductor is given by

$$V_{L_1} = L_1 \frac{di}{dt} \tag{13}$$

Equation (14) gives the inductor current during the ON state, or mode 1, using the inductor voltage from Equation (6) and assuming that all initial conditions are zero.

$$I_{on} = \int_0^{t_{on}=DT} V_L \, dt = \frac{V_{in}DT}{L_1} \tag{14}$$

Correspondingly during the OFF state or mode 2, the current in the inductor is calculated by

$$I_{off} = \int_{t_{on}=DT}^{T} V_L \, dt = \frac{-(V_{in}-V_o)(1-DT)}{L_1} \tag{15}$$

The average current flowing through the inductor will remain constant, although the converter is on and off if it functions in steady-state mode. When the load is connected acrossC_2, from Equations (14) and (15), the gain of the converter is expressed as

$$I_{on} + I_{off} = \frac{V_{in}DT}{L_1} - \frac{(V_{in}-V_o)(1-DT)}{L_1} = 0 \tag{16}$$

$$G_{CCM_{C_2}} = \frac{V_{oC_2}}{V_{in}} = \frac{1}{1-D} \tag{17}$$

At the second stage, the gain of the converter is determined by connecting the load to C_4 as depicted in equivalent circuit Figure 5 and is expressed as

$$G_{CCM_{C_2}} = \frac{V_{oC_4}}{V_{in}} = \frac{2}{1-D} \tag{18}$$

$$G_{jstage} = \frac{V_O}{V_{in}} = \frac{j}{1-D} \tag{19}$$

Where, j is any stage from 1, 2, 3…n

$$V_0 = V_{C_2} + V_{C_4} + V_{C_6} + \cdots V_{C_{j\,stage}} \tag{20}$$

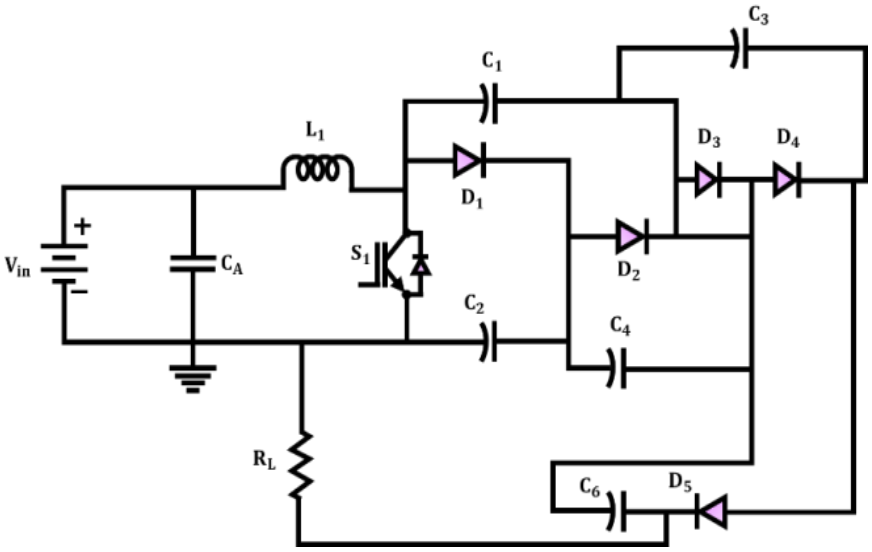

Fig. 2 Higher order boost converter

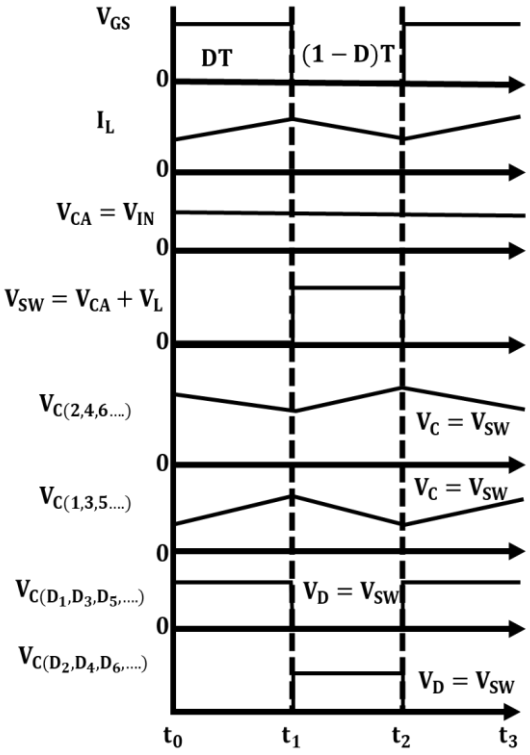

Fig. 3 Higher order boost converter timing diagram

Applying KCL, the average input current and average inductor currents for the proposed converter is given by equation (21) and (22)

$$I_{in} = I_L - I_O \tag{21}$$

$$I_L = I_{in} + I_O \tag{22}$$

$$I_L = I_O(1 + G_{jstage}) \tag{23}$$

$$I_{in} = \frac{j}{1-D} I_O \tag{24}$$

The proposed converter operates on the zero-switch current theory (ZSC). The diodes $D_1, D_2, D_3, D_4,$ and D_5 experience reverse recovery difficulty in the OFF position if the converter cannot follow the current.

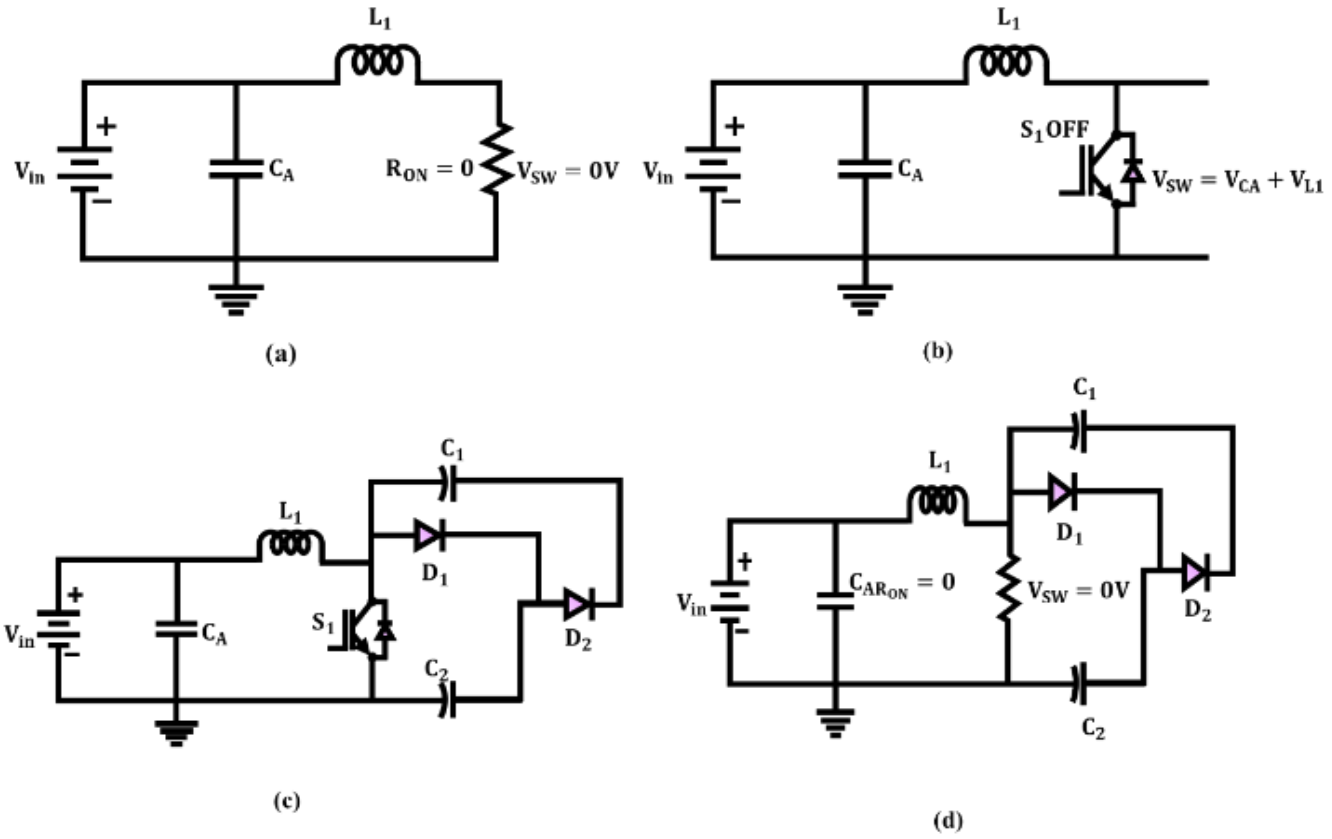

Fig. 4 A higher order boost converter (a) mode 1 and (b) mode 2 (c) charging of output capacitors and (d) discharging of output capacitors

3.2.3. Voltage Stress

The Proposed converter faces voltage stress across the switches when it remains in OFF mode. Figure 2 exhibits three voltage stress compared to the output voltage. The switch stress across the diodes, MOSFET and capacitors in the proposed converter is $j^{-1}V_O$. In the current research, the voltage stress over the switches is comparatively reduced by raising the duty cycle ratio.

$$V_{C_2}, V_{C_4}, V_{C_6} \dots V_{C_j} = V_{D_1}, V_{D_2}, \dots . V_{D_n}, = V_{SW} = \frac{V_O}{j} = \frac{2}{j} V_O(1 - \mathrm{D}) \quad (25)$$

The normalized voltage stress across the power switch $(\frac{V_{sw}}{V_{in}})$ or $(\frac{V_{sw_{stress}}}{V_{in}})$ in accordance with CCM gain and diodes $(\frac{V_{D_{stress(1\dots..n)}}}{V_{in}})$is expressed as

$$\left(\frac{V_{sw_{stress}}}{V_{in}}\right) = \left(\frac{V_{D_{stress(1\dots..n)}}}{V_{in}}\right) = \frac{1}{1-D}$$

(Or)

$$\frac{V_{sw_{stress}}}{V_O} = \frac{2}{j}(1 - D) \quad (26)$$

3.2.4. Current Stress

The normalized inductor current stress $(\frac{I_L}{I_{in}})$ is written as

$$\left(\frac{I_L}{I_{in}}\right) = \frac{G_{jstage}+1}{G_{jstage}} \quad (27)$$

Using a GWO-assisted FOPID controller, the dynamic performance of the higher-order Boost converter is enhanced in terms of reduced overshoot, effective error compensation, and quick settling time.

3.3. Modelling of GWO Assisted FOPID Controller

The FOPID controller, a fractional calculus-based application, is suitable for handling non-linear operations since it offers a better closed-loop response, high stability, excellent flexibility, quick response and better control. This linear PID controller extension is represented as $PI^{\alpha}D^{\beta}$, where the fractional orders of differentiator and integrator are specified as α and β, respectively. The expression for the controller is,

$$C(s) = K_p + K_i s^{-\alpha} + K_d s^{\beta} \quad (28)$$

It is possible to acquire a linear PID controller by equating both α and β values to 1. Moreover, the choice of $(\alpha, \beta) = (0,1)$ gives PD controller, while the choice of $(\alpha, \beta) = (1,0)$ gives PI controller. This controller can also meet five specifications on account of its five adjustable parameters.

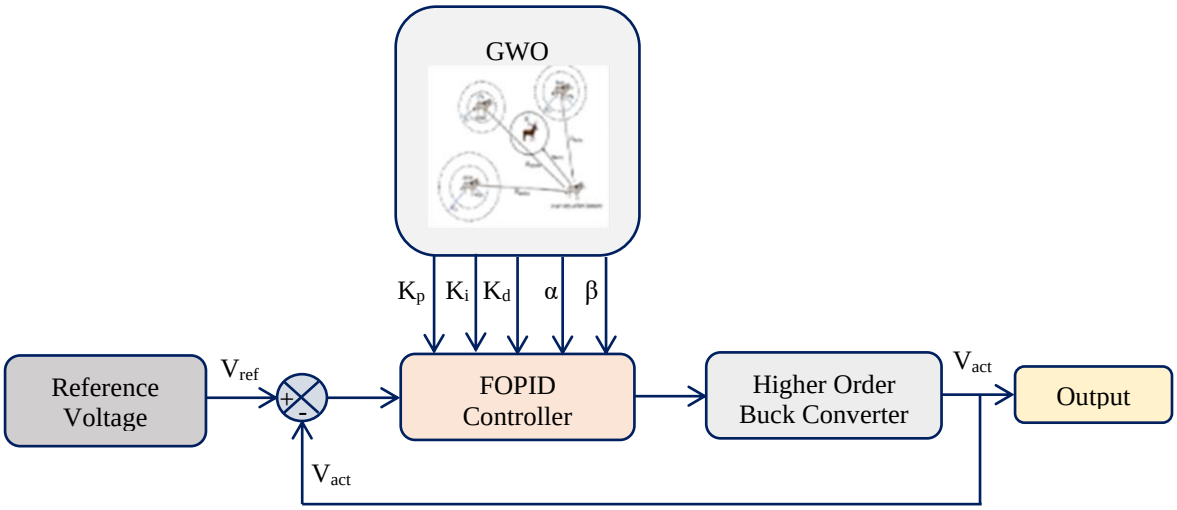

Fig. 5 Structure of GWO assisted FOPID controller

The GWO algorithm is estimated in this work for generating the optimal FOPID controller parameters for higher order Boost converter by minimizing the objective function obtained from the error between V_{act} and V_{ref}. Figure 5 gives the structure of GWO assisted FOPID controller.

3.3.1. GWO Algorithm

The GWO is an effective metaheuristic algorithm devised for emulating the behaviour of wolves while hunting. This algorithm involves a random number of wolves (search agents) that initially track and then approach the location of their prey before hunting it down using an iterative procedure. Every key decision for the wolf pack is made by the alpha wolf, which assumes the role of leader. The direct subordinates of the alpha are the beta wolves, while the delta and omega wolves fit in the lower level of social hierarchy. Along with the group hunting tendency of the grey wolf, its social hierarchy is also considered while designing the GWO algorithm. The different phases of the grey wolf hunting process are,

- Tracing, trailing and encircling the prey.
- Subjugating, persecuting and tormenting the prey until it remains still without motion.
- Finally, the prey is hunted down.

The wolves update their position while attacking their prey, which is expressed as,

$$D_j = |C_j . X_p(t) - X_j(t)| \quad (29)$$

$$X_j(t+1) = X_p(t) - A_j . D_j \quad (30)$$

Here, both $A_j\ (= 2a \cdot r_1)$ and $C_j\ (= 2 \cdot r_2)$ are coefficient vectors, X_p is prey position, X_j is grey wolf position, $a = 2 - 2t/t_{max}$, t refers to the current iteration and both r_1 and r_2 are random parameters. The updated position of both the prey and wolf is given as,

$$X_1 = X_\alpha(t) - A_1 . D_\alpha \quad (31)$$

$$X_2 = X_\beta(t) - A_2 . D_\beta \quad (32)$$

$$X_3 = X_\delta(t) - A_3 . D_\delta \quad (33)$$

$$D_\alpha = |C_1 . X_\alpha(t) - X_j(t)| \quad (34)$$

$$D_\beta = |C_2 . X_\beta(t) - X_j(t)| \quad (35)$$

$$D_\delta = |C_3 . X_\delta(t) - X_j(t)| \quad (36)$$

$$X_j(t+1) = (X_1 + X_2 + X_3)/3 \quad (37)$$

The flowchart of GWO is presented in Figure 6. The GWO algorithm aids with acquiring the unknown FOPID controller parameters $(K_p, K_i, K_d, \lambda\ and\ \mu)$ by performing optimization with the Integral of Square Error (ISE) objective function. The ISE objective function is defined as,

$$ISE = \int_0^t e^2(t)\, dt \quad (38)$$

The ISE offers more practical significance since it prioritizes large error penalization over smaller ones. The error is evaluated as $e(t) = V_{ref} - V_{act}$, where the time t is selected as a value either greater or equal to the settling time.

3.4. Modelling of DFIG Based WECS

The wind kinetic energy is harnessed to generate electric power by the WECS. The following equations describe the wind turbine characteristics,

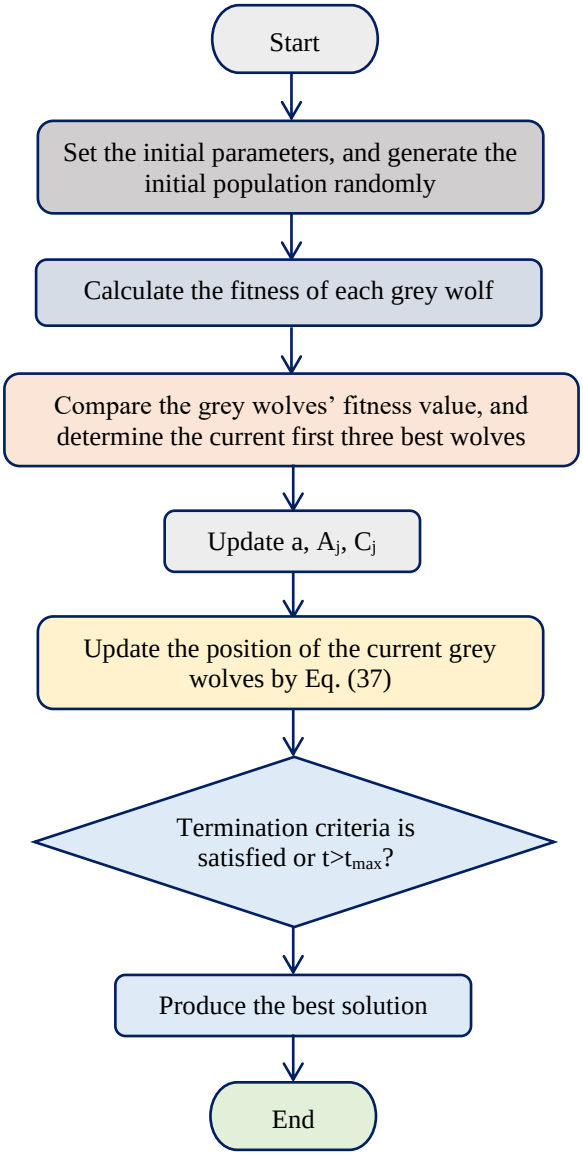

Fig. 6 Flowchart of GWO

$$T_m = \frac{0.5\rho\pi R^2 C_p(\lambda,\beta)V_{wind}^3}{\omega_{WT}} \quad (39)$$

$$C_p(\lambda,\beta) = 0.645\left(\frac{116}{\lambda_i} - 0.4\beta - 5\right)e^{-21/\lambda_i} \quad (40)$$

$$\lambda_i = \frac{1}{1/\lambda + 0.08\beta - 0.035/(\beta^3+1)} \quad (41)$$

Where, $\beta, \lambda, \rho, C_p$ and R refers to pith angle, tip speed ratio, air density, power coefficient and blade radius. The mechanical torque, wind speed, along with wind turbine speed is specified by $T_m, V_{wind}\omega_{WT}$. Recently, wind farms have been integrated into the electric power system with DFIG-based wind generation systems. The following equation gives the modelling of DFIG in $\alpha\beta$ stationary reference frame.

$$\begin{cases} \overrightarrow{V_s} = R_s\overrightarrow{\imath_s} + \dot{\overrightarrow{\Psi_s}} + j\omega_s\overrightarrow{\Psi_s} \\ \overrightarrow{V_r} = R_r\overrightarrow{\imath_r} + \dot{\overrightarrow{\Psi_r}} + j(\omega_s - \omega_g)\overrightarrow{\Psi_r} \end{cases} \quad (42)$$

$$\begin{cases} \overrightarrow{\Psi_s} = L_s\overrightarrow{\imath_s} + L_m\overrightarrow{\imath_r} \\ \overrightarrow{\Psi_r} = L_r\overrightarrow{\imath_r} + L_m\overrightarrow{\imath_s} \end{cases} \quad (43)$$

$$T_e = \frac{3n_p}{2}Re(j\overrightarrow{\Psi_s}\,\overrightarrow{\imath_s}) \quad (44)$$

The rotor and stator voltage vectors are given by $\overrightarrow{V_r} = V_{\alpha r} + j\mu_{\beta r}$ *and* $\overrightarrow{V_s} = V_{\alpha s} + jV_{\beta s}$, whereas the rotor and stator current vectors are given by $\overrightarrow{\imath_r} = i_{\alpha r} + j\mu_{\beta r}$ *and* $\overrightarrow{\imath_s} = i_{\alpha s} + ji_{\beta s}$. In work, the PI controller is used to maintain a constant power supply from the DFIG based WECS.

3.5. Modelling of ESS with Isolated Bidirectional Battery

Energy storage system plays a dominant role in RES. Rarely do energy supply and demand match up at any time of day. Thus, storing excess energy when energy production exceeds consumption becomes necessary. In contrast, when a surplus of energy is needed but not enough energy is produced, an energy storage device supplies it. In this research, lithium-ion battery is considered. Equation (45) determines the instantaneous state of charge (SOC), which regulates how the battery charges and discharges.

$$SOC(t) = SOC(t-1).\left(1 - \frac{\sigma.\Delta t}{24}\right) + \frac{I_{bat}(t).\Delta t.\eta_{bat}}{C_{bat}} \quad (45)$$

At any time$t$, SOC is the function of the previous SOC$(t-1)$. σ denotes the battery's self-discharge, an electrochemical process that causes the batteries to deplete fast even when electrical consumers are not connected and are considered 0.2% per day. Δt Is the hourly time step, I_{bat} is battery current for t^{th} hour, η_{bat} is the battery charging and discharging efficiency and $C_{bat}$is the nominal capacity of the battery. The battery's efficiency varies depending on the SOC, and it is assumed to be 1 when the battery is discharged and 0.8 for being charged. The current obtained from the battery by integrating PV with WT is

$$I_{bct}(t) = \frac{P_{PV}(t)+P_{WT}(t)-P_{Load}(t)}{V_{bct}} \quad (46)$$

Where $V_{bct}$is the individual battery's nominal voltage ofP_{PV}, P_{WT}, and P_{Load} are the power obtained from PV, WT and load. The high-power transfer for the battery is achieved using the Isolated BDC illustrated in Figure 7. The Isolated BDC is a Dual Active Bridge (DAB) converter, which entails two full-bridge converters in its structure. The power transmission using Isolated BDC is expressed as,

$$P_{transmission} = \frac{nV_1V_2}{2f_sL}\left[\left(d(1-d) - \frac{1}{2}d_1(1-d_1-2d)\right)\right] \quad (47)$$

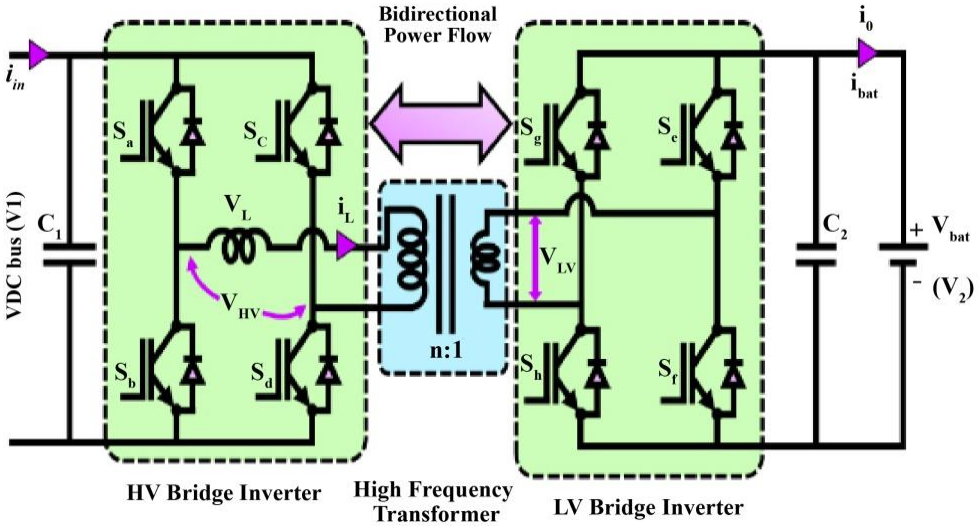

Fig. 7 Structure of isolated BDC

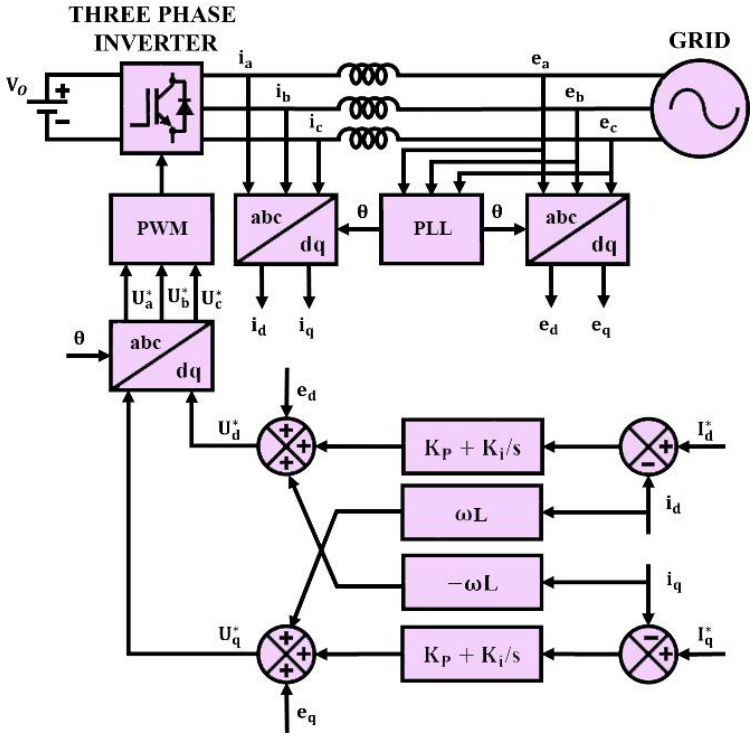

Fig. 8 Grid voltage synchronization

The circulating power is represented as,

$$P_{circulating} = \frac{nV_1V_2}{16f_sL}[k(1-d_1)+(2d-1)]^2 \quad (48)$$

The converter stress is represented as,

$$i_{stress} = \frac{nV_2}{4f_sL}\left[\left(k(1-d_1)+(2d_1-2d-1)\right)\right] \quad (49)$$

Where, n is the transformer turns ratio, the leakage inductance is specified as L, the operating frequency is f_s, low voltage is specified as V_2 and high voltage is specified as V_1. The term k refers to the voltage conversion ratio, and the terms d *and* d_1 refers to the phase shift ratio.

3.6. Grid Voltage Synchronization

This study proposes a PI controller-based current control approach for grid voltage synchronization, as illustrated in Figure 8. This approach delivers a quicker response and is less sensitive to interruptions in grid voltage. The PI controller minimizes the error obtained by comparing the desired reference current to the actual VSI output current.

Table 1. Parameter specifications

Solar cell	
Parameters	Ratings
No. of Panels	20 panels
Peak Power	10kW
Capacity	500W
Short circuit voltage V_{SC}	12V
Short circuit current I_{SC}	41.6A
Open circuit voltage V_{OC}	22.6V
Series connected solar PV cells	36
WECS	
No. of Turbines	1
Power	10kW
Voltage	575V
Speed Range	4m/s – 16m/s
HIGHER ORDER BOOST CONVERTER	
C_A, C_1, C_2	180µF
C_3, C_4, C_6	2200µF
L_1	3.7mH
Switching frequency f	10kHz

Table 2. Comparison of converter efficiency and voltage gain

DC-DC Converters	Higher Order Boost Converter	Cuk Converter [26]	Buck-Boost Converter [27]	Boost Converter [28]
Voltage Gain	8	3	6	1.5
Efficiency (%)	98.4	85	85	80

Table 3. Transient response parameters of the controller's comparison

Algorithm/ Controller	GWO/ PID [29]	SFS/ PID [29]	PSO/ PID [29]	IWO/ PID [29]	GWO/ FOPID
Rise time (s)	0.171	0.638	0.409	0.493	0.058
Settling time (s)	0.254	1.06	2.38	1.95	0.15
Over Shoot (%)	1.06	0	25.5	7.16	0.42

The overall error is minimized by using the proportional term, which is the product of error and proportional gain. The remnant steady-state error is eliminated using the integral term obtained by multiplying the error with the integral gain.

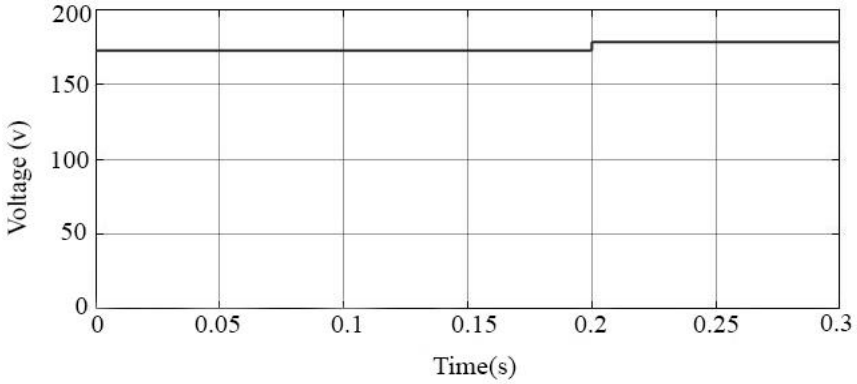

(a)

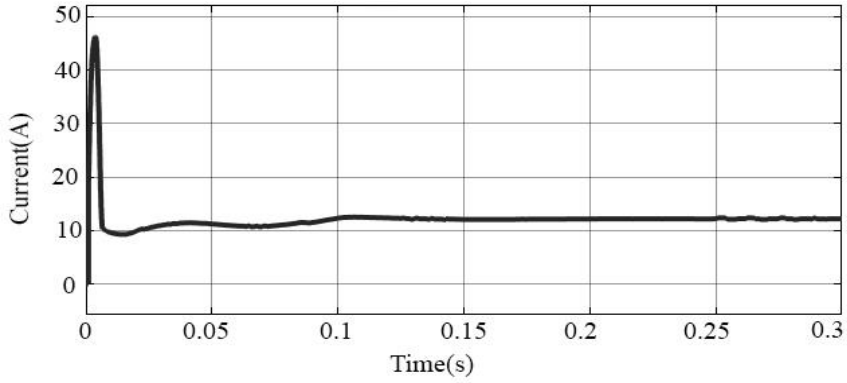

(b)

Fig. 9 PV system (a) output voltage waveform and (b) output current waveform

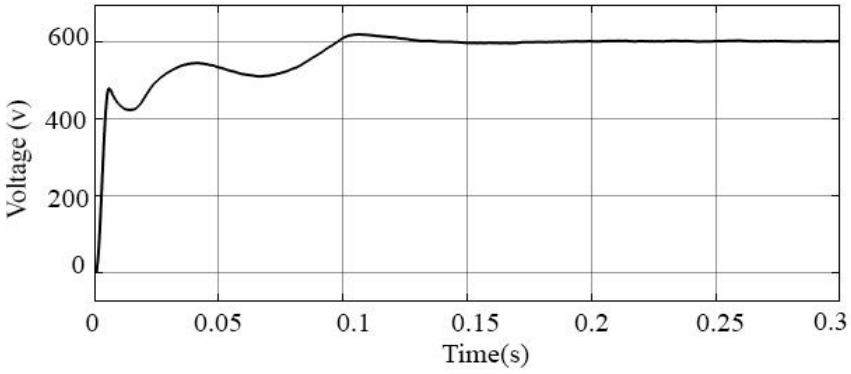

(a)

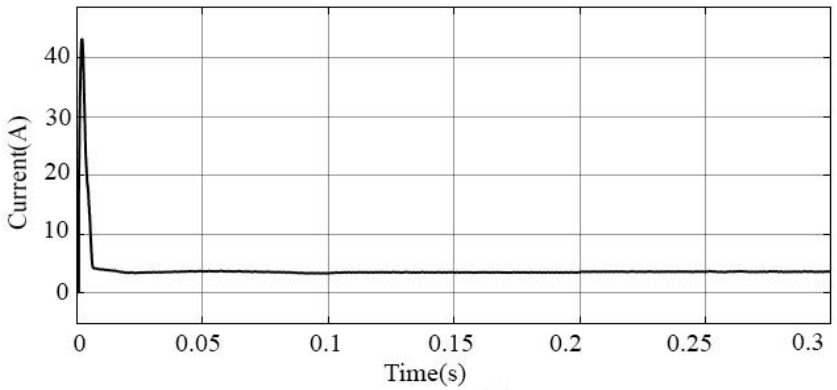

(b)

Fig. 10 Higher order boost converter (a) output voltage waveform and (b) output current waveform

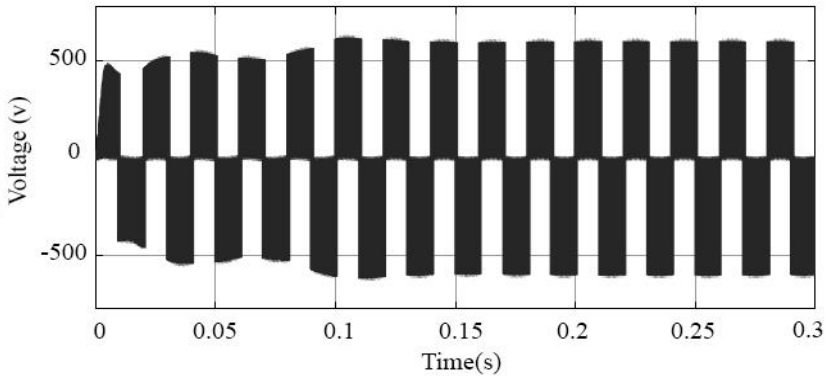

(a)

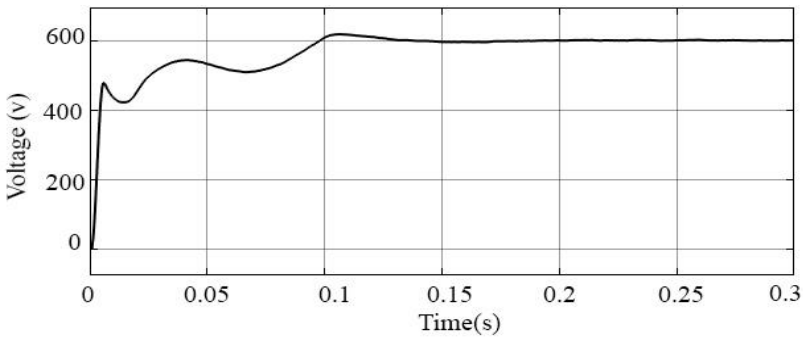

(b)

Fig. 11 Output voltage waveform (a) DFIG and (b) PWM rectifier

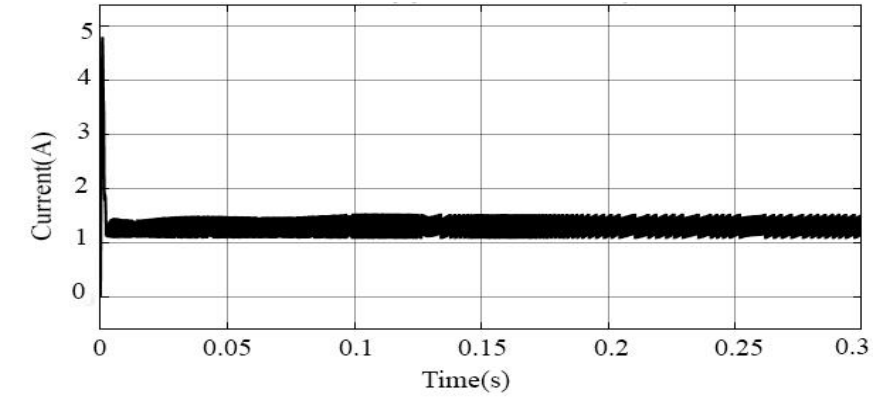

(a)

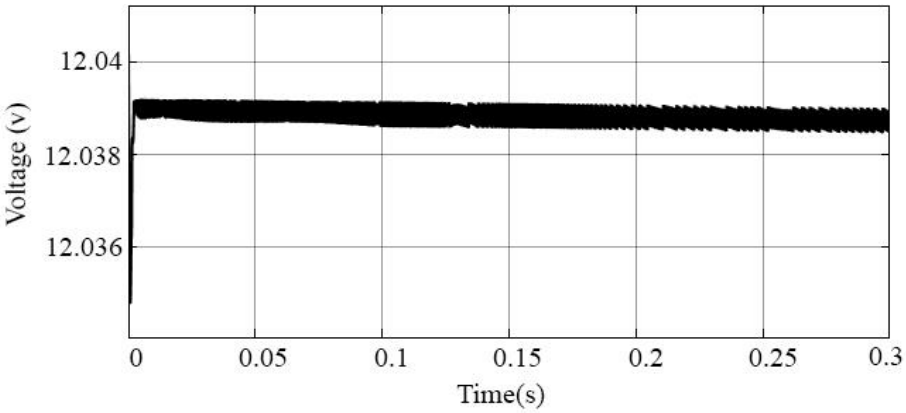

(b)

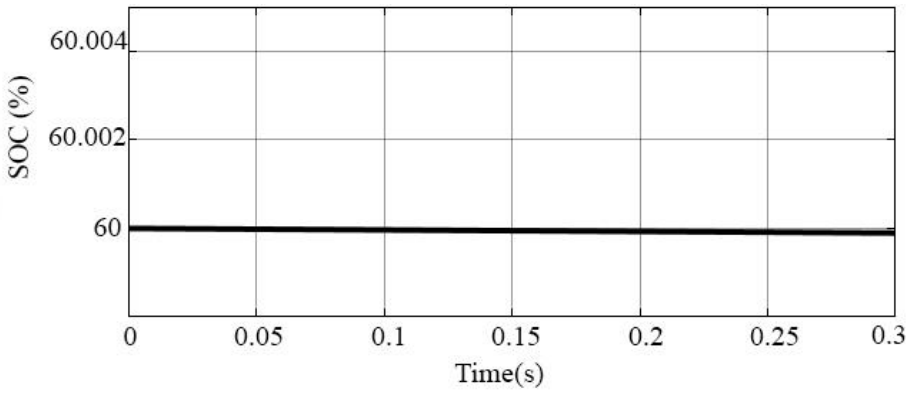

(c)

Fig. 12 Battery waveforms (a) current, (b) voltage, and (c) SOC

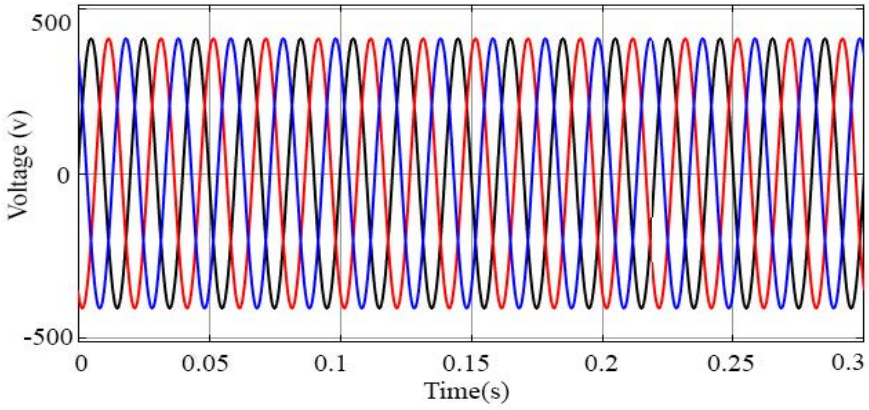
500
0
-500
Voltage (v)
0
0.05
0.1
0.15
0.2
0.25
0.3
Time(s)

(a)

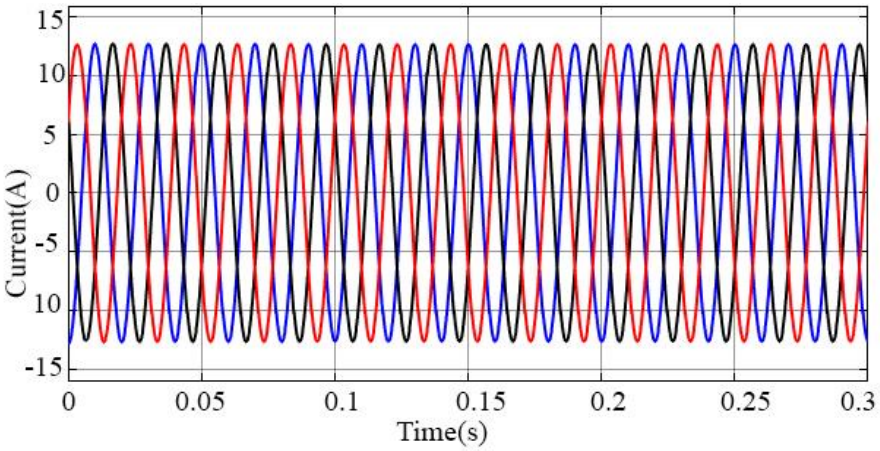
15
10
5
0
-5
10
-15
Current(A)
0
0.05
0.1
0.15
0.2
0.25
0.3
Time(s)

(b)

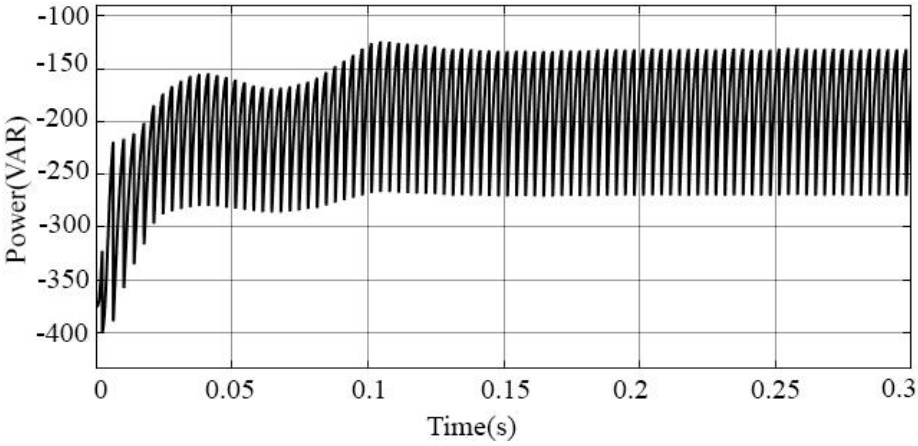
-100
-150
-200
-250
-300
-350
-400
Power(VAR)
0
0.05
0.1
0.15
0.2
0.25
0.3
Time(s)

(c)

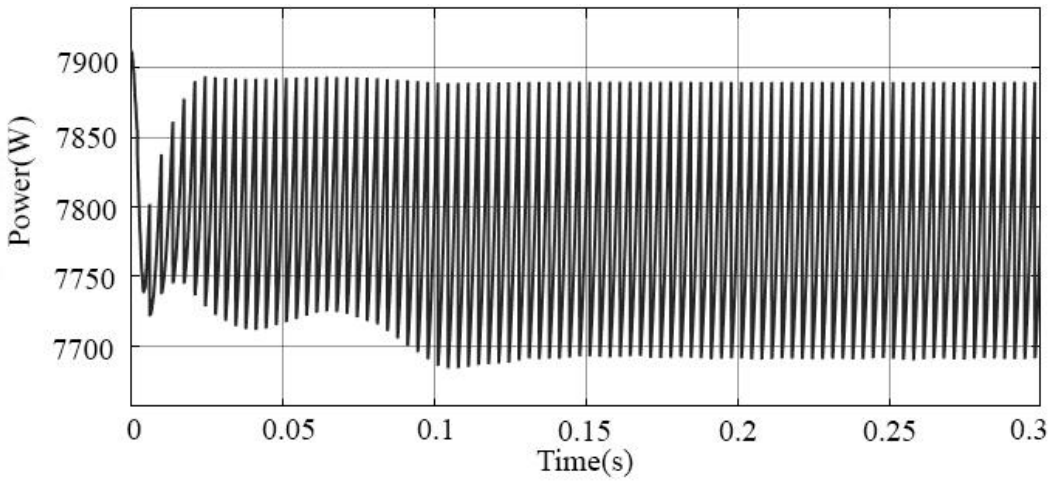

(d)

Fig. 13 (a) Grid voltage waveform, (b) Grid current waveform, (c) Reactive power waveform, and (d) Real power waveform

The PWM approach is employed to control the utility grid's active and reactive power components. The proposed grid voltage synchronization technique has an excellent steady-state response and minimum harmonics.

4. Results and Discussions

The design of a DC microgrid that includes a hybrid power system of PV and WECS with appropriate control approaches for enhancing the overall voltage stability and power quality is proposed in this study.

Moreover, the balance of power at the time of shortages in supply from both primary power sources is resolved by integrating ESS into the proposed microgrid structure. The simulation model for the proposed microgrid structure is created in MATLAB and executed to ascertain the microgrid operation. The parameters used for designing the simulation model are given in Table 1.

4.1. PV system

The solar panel output voltage remains at 172.5V for 0.2 seconds before increasing to 178V, as seen in Figure 9(a). This abrupt variation in voltage level is attributed to the variation in operating conditions such as temperature and solar intensity. This variable and intermittent nature of the PV system leads to instability issues in the microgrid in the absence of a suitable control technique.

An input current to the higher order Boost converter, i.e., the PV panel output current, is observed to be 12 V from Figure 9(b). Furthermore, it is also observed that the current is not constant and is affected by minor distortions.

The voltage gain of the suggested higher-order Boost converter is 1:8, and its efficiency is 98.4%, much greater than that of the other converters taken into consideration in the list. The robustness of the proposed GWO-assisted FOPID controller is analysed in terms of rise time, settling time and overshoot with other optimization algorithms like PSO, Stochastic Fractal Search (SFS) and Invasive Weed Optimization (IWO). The GWO-assisted FOPID is noted to have outperformed all the other control techniques with a settling time of 0.15s, a rise time of 0.058s and an overshoot of 0.42%.

4.2. DFIG-based WECS

Similar to the PV system, the WECS is also a variable power source characterised by uncertainty in its output. DFIG-based WECS is considered in this study, and the square-type three-phase output voltage waveform obtained from the DFIG-based WECS is provided in Figure 11(a). The DFIG output voltage varies in accordance with the variation in wind speed. Therefore, the output voltage waveform is observed to be not stable.

4.3. Energy Storage System

The performance of the ESS is evaluated based on battery current, voltage and SOC waveforms given in Figure 12. From the graphs provided in the figure, it is observed that the magnitude of the current is 1.5A, and the magnitude of the battery voltage is 12V. Moreover, the SOC of the battery is observed to be 60%.

4.4. Grid Synchronization

The role of an effective grid voltage synchronization approach is significant when integrating the power generated from both the RESs to the utility grid. The PI controller's integral and proportional terms eliminate the VSI output's steady-state error. Moreover, the differences in the amplitude, frequency and phase between the grid voltage and the inverter voltage are completely minimized using the proposed linear current controller-based approach.

The grid voltage range is -400V to +400V, while the grid current is in the range of -13V to +13V, as seen in Figure 13. Moreover, the real and reactive power waveforms are given in Figure 13 (d) and 13(c), respectively.

5. Conclusion

An objective of this work is to devise a suitable control technique for enhancing the voltage stability of a hybrid power system (WECS- PV-Battery) based DC microgrid. This work mainly aims at facilitating the increased penetration of RESs for power production by overcoming the limitations associated with RESs intermittency. Thereby, in the case of a PV system, both a higher-order Boost converter and GWO-assisted FOPID controller are chosen for steadying its output voltage.

The PI controller provides the necessary error compensation for stabilizing the DFIG based WECS output. Moreover, an isolated BDC is chosen over its non-isolated BDC counterpart for integrating the battery into the DC bus. In addition to its excellent bidirectional power flow capability, the isolated BDC offers high power density, symmetrical topology and soft-switching.

A PI controller-based linear current control approach is used for accomplishing grid voltage synchronization. From the MATLAB simulation results, it is observed that the higher-order Boost converter, with the assistance of an optimized FOPID controller, operates at an efficiency of 98.4%.

References

[1] K. S. Kavin, and P. Subha Karuvelam, "PV-based Grid Interactive PMBLDC Electric Vehicle with High Gain Interleaved DC-DC SEPIC Converter," *IETE Journal of Research*, pp. 1-15, 2021. [CrossRef]

[2] Itbar Khan et al., "Analyzing Renewable and Non-Renewable Energy Sources for Environmental Quality: Dynamic Investigation in Developing Countries," *Mathematical Problems in Engineering*, 2021. [CrossRef]

[3] Kavitha P, Dr. SubhaKaruvelam P, and K. S. Kavin, "Energy Management of AC Grid by the Solar PV System Using Landsman Converter," *SSRN*, 2020. [CrossRef]

[4] Md. Arif Hossain et al., "Multi-Objective Hybrid Optimization for Optimal Sizing of a Hybrid Renewable Power System for Home Applications," *Energies*, vol. 16, no. 1, p. 96, 2022. [CrossRef]

[5] Gabriel R. Broday, Luiz A. C. Lopes, and Gilney Damm, "Exact Feedback Linearization of a Multi-Variable Controller for a Bi-Directional DC-DC Converter as Interface of an Energy Storage System," *Energies*, vol. 15, no. 21, p. 7923, 2022. [CrossRef]

[6] Yonghao Gui et al., "Large-Signal Stability Improvement of Dc-Dc Converters in Dc Microgrid," *IEEE Transactions on Energy Conversion*, vol. 36, no. 3, pp. 2534-2544, 2021. [CrossRef]

[7] V. Devaraj, and M. Kumaresan, "An Elite LOA-TFWO Approach for Load-Frequency Control of Islanded Micro-Grids Incorporating Renewable Sources," *International Journal of Engineering Trends and Technology*, vol. 70, no. 10, pp. 166-187, 2022. [CrossRef]

[8] Chandra Sekhar Nalamati, and Rajesh Gupta, "Isolated Bidirectional Battery Converter Control for Standalone Solar PV Applications," *2018 IEEMA Engineer Infinite Conference (eTechNxT)*, pp. 1-5, 2018. [CrossRef]

[9] Gautam A. Raiker, Umanand Loganathan, and Subba Reddy B, "Current Control of Boost Converter for PV Interface with Momentum-Based Perturb and Observe MPPT," *IEEE Transactions on Industry Applications*, vol. 57, no. 4, pp. 4071-4079, 2021. [CrossRef]

[10] Muhammad Saqib Ali et al., "Performance Improvement of Three-Phase Boost Power Factor Correction Rectifier through Combined Parameters Optimization of Proportional-Integral and Repetitive Controller," *IEEE Access*, vol. 9, pp. 58893-58909, 2021. [CrossRef]

[11] Zhenbao Pan et al., "Combined Resonant Controller and Two-Degree-of-Freedom PID Controller for PMSLM Current Harmonics Suppression," *IEEE Transactions on Industrial Electronics*, vol. 65, no. 9, pp. 7558-7568, 2018. [CrossRef]

[12] Baran Hekimoğlu, "Optimal Tuning of Fractional Order PID Controller for DC Motor Speed Control via Chaotic Atom Search Optimization Algorithm," *IEEE Access*, vol. 7, pp. 38100-38114, 2019. [CrossRef]

[13] J. Shirisha et al., "Deep Learning-Based Image Processing Approach for Irradiance Estimation in MPPT Control of Photovoltaic Applications," *SSRG International Journal of Electrical and Electronics Engineering*, vol. 9, no. 9, pp. 32-37, 2022. [CrossRef]

[14] Kalal Muralidhar Goud, and Shyam Krishna Nagar, "Fractional Order PD Controller Design for Non-Monotonic Phase Systems," *International Journal of Automation and Control*, vol. 9, no. 2, pp. 130-142, 2015. [CrossRef]

[15] K. Muralidhar Goud, and C. Srisailam, "Control Quality Enhancement of Inverted Pendulum Using Fractional Controller," *Innovations in Electrical and Electronics Engineering*, *Springer*, Singapore, pp. 705-713. 2020. [CrossRef]

[16] K Muralidhar Goud et al., "Stability analysis of Automatic Voltage Regulator using Fractional Order Controller," *Turkish Journal of Computer and Mathematics Education (TURCOMAT)*, vol. 12, no. 2, pp. 780-787, 2021. [CrossRef]

[17] Suman Saha et al., "Fractional Order Phase Shaper Design with Bode's Integral for ISO-Damped Control System," *ISA Transactions*, vol. 49, no. 2, pp. 196-206, 2010. [CrossRef]

[18] Saptarshi Das et al., "On the Selection of Tuning Methodology of FOPID Controllers for the Control of Higher Order Processes," *ISA Transactions*, vol. 50, no. 3, pp. 376-388, 2011. [CrossRef]

[19] Mangala R. Dhotre, Prashant V. Thakre, and Vijay M. Deshmukh, "A Novel Method for Implementing MPPT Based Photovoltaic Closed Loop Flyback Inverter with STM32F407VG Controller using Waijung Tool," *International Journal of Engineering Trends and Technology*, vol. 70, no. 8, pp. 194-205, 2022. [CrossRef]

[20] Jun-Yi Cao, Jin Liang, and Bing-Gang Cao, "Optimization of Fractional Order PID Controllers Based on Genetic Algorithms," *2005 International Conference on Machine Learning and Cybernetics, IEEE*, vol. 9, pp. 5686-5689, 2005. [CrossRef]

[21] Erdinc Sahin, Mustafa Sinasi Ayas, and Ismail Hakki Altas, "A PSO Optimized Fractional-Order PID Controller for a PV System with DC-DC Boost Converter," *2014 16th International Power Electronics and Motion Control Conference and Exposition, IEEE*, pp. 477-481, 2014. [CrossRef]

[22] K. Vanchinathan, and K. R. Valluvan, "A Metaheuristic Optimization Approach for Tuning of Fractional-Order PID Controller for Speed Control of Sensorless BLDC Motor," *Journal of Circuits, Systems and Computers*, vol. 27, no. 8, p. 1850123, 2018. [CrossRef]

[23] Venkata Yaramasu et al., "High-Power Wind Energy Conversion Systems: State-of-the-Art And Emerging Technologies," *Proceedings of the IEEE*, vol. 103, no. 5, pp. 740-788, 2015. [CrossRef]

[24] S. Sami, "Impact of Nanofluids on Performance of Solar Photovoltaic-Thermal Panel and Heat Pipe Hybrid System," *SSRG International Journal of Thermal Engineering*, vol. 7, no. 1, pp. 5-20, 2021. [CrossRef]

[25] Paulo Sergio Nascimento Filho et al., "Modeling and Experimental Evaluation of Energy Storage Emulator for Microgrids Application," *IEEE Journal of Emerging and Selected Topics in Power Electronics*, vol. 9, no. 6, pp. 6662-6670, 2021. [CrossRef]

[26] Francarl Galea et al., "Design of a High Efficiency Wide Input Range Isolated Cuk DC-DC Converter for Grid Connected Regenerative Active Loads," *CORE*, 2011.

[27] S. Saravanan, P. Usha Rani, and Mohan P. Thakre, "Evaluation and Improvement of a Transformerless High-Efficiency DC–DC Converter for Renewable Energy Applications Employing a Fuzzy Logic Controller," *MAPAN*, pp. 1-20, 2022. [CrossRef]

[28] Farzam Nejabatkhah et al., "Modeling and Control of a New Three-Input DC–DC Boost Converter for Hybrid PV/FC/Battery Power System," *IEEE Transactions on Power Electronics*, vol. 27, no. 5, pp. 2309-2324, 2012. [CrossRef]

[29] Jeetendra Agarwal et al., "Analysis of Grey Wolf Optimizer Based Fractional Order PID Controller in Speed Control of DC Motor," *Microsystem Technologies*, vol. 24, no. 12, pp. 4997-5006, 2018. [CrossRef]

[30] M. Usharani et al., "An Optimized Deep Learning Model Based PV Fault Classification for Reliable Power Generation," *SSRG International Journal of Electrical and Electronics Engineering*, vol. 9, no. 9, pp. 23-31, 2022. [CrossRef]

[31] Preeti Warrier, and Pritesh Shah, "Optimal Fractional PID Controller for Buck Converter Using Cohort Intelligent Algorithm," *Applied System Innovation*, vol. 4, no. 3, p. 50, 2021. [CrossRef]

[32] V. Fernão Pires et al., "Dual Output and High Voltage Gain DC-DC Converter for PV and Fuel Cell Generators Connected to DC Bipolar Microgrids," *IEEE Access*, vol. 9, pp. 157124-157133, 2021. [CrossRef]

[33] Norain Sahari et al., "Development of Hybrid Photovoltaic and Thermoelectric Generator for Energy Harvesting," *International Journal of Engineering Trends and Technology*, vol. 70, no. 8, pp. 284-291, 2022. [CrossRef]

[34] Sevilay Tufenkci et al., "Disturbance Rejection FOPID Controller Design in V-Domain," *Journal of Advanced Research*, vol. 25, pp. 171-180, 2020. [CrossRef]

[35] Vijay Chand Ganti et al., "DFIG-Based Wind Power Conversion with Grid Power Leveling for Reduced Gusts," *IEEE Transactions on Sustainable Energy*, vol. 3, no. 1, pp. 12-20, 2012. [CrossRef]